materials

MDPI

Article

Dual Oxygen Defects in Layered $La_{1.2}Sr_{0.8-x}Ba_xInO_{4+\delta}$ (x = 0.2, 0.3) Oxide-Ion Conductors: A Neutron Diffraction Study

Loreto Troncoso [1,2,*], Carlos Mariño [2,3], Mauricio D. Arce [4] and José Antonio Alonso [1]

1 Instituto de Ciencia de Materiales de Madrid, CSIC, Cantoblanco, 28049 Madrid, Spain; ja.alonso@icmm.csic.es
2 Instituto de Materiales y Procesos Termomecánicos, Universidad Austral de Chile, General Lagos, 2086, 5111187 Valdivia, Chile; carlos.marino@usach.cl
3 Departamento de Metalurgia, USACH, Ave Ecuador 3469, 9170124 Santiago, Chile
4 CNEA-CONICET, Centro Atómico Bariloche, Av. Bustillo 9500, S. C. de Bariloche, 8400 Río Negro, Argentina; mauricio.arce@gmail.com
* Correspondence: loreto.troncoso@uach.cl

Received: 12 April 2019; Accepted: 15 May 2019; Published: 17 May 2019

Abstract: The title compounds exhibit a K_2NiF_4-type layered perovskite structure; they are based on the $La_{1.2}Sr_{0.8}InO_{4+\delta}$ oxide, which was found to exhibit excellent features as fast oxide-ion conductor via an interstitial oxygen mechanism. These new Ba-containing materials were designed to present a more open framework to enhance oxygen conduction. The citrate-nitrate soft-chemistry technique was used to synthesize such structural perovskite-type materials, followed by annealing in air at moderate temperatures (1150 °C). The subtleties of their crystal structures were investigated from neutron powder diffraction (NPD) data. They crystallize in the orthorhombic *Pbca* space group. Interstitial O3 oxygen atoms were identified by difference Fourier maps in the NaCl layer of the K_2NiF_4 structure. At variance with the parent compound, conspicuous oxygen vacancies were found at the O2-type oxygen atoms for x = 0.2, corresponding to the axial positions of the InO_6 octahedra. The short O2–O3 distances and the absence of steric impediments suggest a dual oxygen-interstitial mechanism for oxide-ion conduction in these materials. Conductivity measurements show that the activation energy values are comparable to those typical of ionic conductors working by simple vacancy mechanisms (~1 eV). The increment of the total conductivity for x = 0.2 can be due to the mixed mechanism driving both oxygen vacancies and interstitials, which is original for these potential electrolytes for solid-oxide fuel cells.

Keywords: oxygen-ion conductor; solid electrolyte; layered perovskite; oxygen interstitials; oxygen vacancies; activation energy; neutron powder diffraction

1. Introduction

Fuel cells are electrochemical devices capable of transforming the chemical energy stored in a fuel directly into electricity. The direct combustion of a fuel, e.g., hydrogen, involves a direct transfer of electrons from H to the oxidant, e.g., oxygen, taking advantage of the combustion heat as the only profit of the direct chemical reaction. The efficiency is restricted to the Carnot cycle [1] in the case of direct combustion. A fuel cell takes advantage of the electron transfer between H_2 and O_2 molecules, which is achieved by separating the oxidation and reduction semi-reactions with an electrolyte; here the combustion heat is just a side product. There are several types of fuel cells, of which solid-oxide fuel cells (SOFC) exhibit the highest performance; they are promising for stationary applications [2–4]. In a SOFC, the anode, the cathode, and the electrolyte are metal oxides; therefore, the operating

temperatures are subject to the oxide-ion conduction capacity of the electrolyte. Hence, high operating temperatures (typically around 1000 °C) are required to stimulate this ionic conductivity. Many inconveniences arise from these high operation temperatures, therefore a reduction is desirable to an intermediate-temperature range between 600–850 °C. The preservation of the characteristic high efficiency requires the development of novel materials with improved properties, in particular, novel electrolytes with enhanced ionic conductivity.

The design of these materials should have strict requirements such as an oxygen-ion transport with low activation energy, low electrical resistance, and proper electrochemical kinetics. The commercial and most studied ionic conductors are based on fluorite and perovskite-type structures ($Zr_{1-x}Y_xO_{2-\delta}$, $Ce_{1-x}GdO_{2-\delta}$, $La_{1-x}Sr_xGa_{1-y}Mg_yO_{3-\delta}$) [5–7]. All of them exhibit oxygen ion conductivity values of $\sigma \geq 0.10$ S/cm between 700 and 1000 °C. These exceptional conductivity values are achieved through the creation of vacancies in their framework. However, there are many examples of SOFC with alternative electrolytes working successfully below 800 °C [8–14].

Various alternative frameworks have been described, such as apatites [15] or garnets with $La_xY_{3-x}Fe_5O_{12+\delta}$ composition, where the oxide-ion conduction is based on an excess oxide-ion concentration mechanism [16].

Recently, rare-earth perovskites with K_2NiF_4-type structure have been described to exhibit ionic conduction. These layered structures contain an open interlayer space where an appreciable number of interstitial oxygen atoms can be hosted; therefore, they seem to be a suitable alternative to be used as electrolytes in SOFCs [17–20]. However, the conductivity of these materials is still well below the limits for them to be used as electrolytes in an SOFC system, i.e., below 0.10 S/cm at 700–1000 °C.

The atomic arrangement A_2BO_4 is constituted by single layers of perovskite consisting of corner-sharing BO_6 octahedra, which alternate with a NaCl-type layer of AO atoms. There are two types of oxygens; the equatorial O1 oxygen atoms link the BO_6 octahedra in the basal plane, while the axial O2 oxygen atoms connect the perovskite layers with the AO layer. The interstitial atoms, responsible for the oxide-ions conduction, are found in the sodium chloride type layer, only coordinated by the A cations [21]. In previous studies we described $La_{1+x}Sr_{1-x}InO_{4+\delta}$ (x = 0.1, 0.2) and $SrIn_{1-x}B_xO_{4+\delta}$ (B = Zr, Ti) oxides as possible solid electrolytes for SOFCs [22,23]. The best electrolyte proved to be $La_{1.2}Sr_{0.8}InO_{4.11}$(1), exhibiting extremely low activation energy of only 0.51 eV for the conduction mechanism via interstitials at low temperatures (T< 650 °C), significantly smaller than those of other electrolytes working with a vacancy mechanism, typically of 1 eV.

In these layered K_2NiF_4-type materials, the strategy to induce the accommodation of oxygen interstitials in the NaCl layers is the creation of a positive charge unbalance at La, Sr positions; the mentioned $La_{1.2}Sr_{0.8}$ stoichiometry implies the nominal incorporation of 0.1 oxygen atoms in the interlayer space, assuming trivalent La and In and divalent Sr ions.

Based on these results, in the present work we describe the synthesis and characterization of a new family of oxides with composition $La_{1.2}Sr_{0.8-x}Ba_{0.2}InO_{4\pm\delta}$ (x = 0.2, 0.3), where the introduction of Ba instead of Sr ions aims to expand the NaCl-type layer of the structure in which the ionic conduction takes place. Through a neutron powder diffraction (NPD) study we unveiled a dual defect mechanism for conduction, since both oxygen vacancies concerning the axial octahedral positions, as well as interstitial oxygen atoms where found in the interlayer space.

2. Experimental Section

2.1. Synthesis

$La_{1.2}Sr_{0.8-x}Ba_xInO_{4+\delta}$ (x = 0.2, 0.3, 0.4) oxides were prepared via a citrate-nitrate route. Stoichiometric amounts of analytical grade $Sr(NO_3)_2$ (99 at.%, Strem Chemicals), $La(NO_3)_3{\cdot}6H_2O$ (99.9 at.%, Alfa Aesar), $Ba(NO_3)_2$ (99 at.% Merck), and $In(NO_3)_3{\cdot}9H_2O$ (99.99 at.% Alfa Aesar) were dissolved under stirring in 250 mL of 10% citric-acid (Panreac) aqueous solution with several droplets of concentrated HNO_3 (J.T. Baker) on a porcelain capsule. This mixture was slowly evaporated on a

hot plate with a magnetic stirrer at 300 °C, leading to organic resins where a random distribution of the involved cations was obtained. The resins were dried at 120 °C in a laboratory stove (Heraeus) and slowly decomposed on a muffle at temperatures up to 600 °C for 12 h (JH Hornos). Subsequent treatment at 800 °C for 2 h ensured the total elimination of all the organic materials and nitrates. Final heating at 1150 °C for 12 h gave rise to well-crystallized, homogeneous samples.

2.2. Structural Characterization

The identification and characterization of the final products were carried out by X-ray diffraction (XRD) for phase identification and to assess phase purity using a Bruker-axs D8 diffractometer (40 kV, 30 mA), controlled by DIFFRACTplus software, in the Bragg–Brentano reflection geometry with CuK_α radiation (λ = 1.5418 Å). Neutron powder diffraction (NPD) data were collected in the High-Resolution Powder Diffractometer for Thermal Neutrons (HRPT) at the Swiss Spallation Neutron Source in the Paul Scherrer Institute (SINQ-PSI) Switzerland with a neutron wavelength λ = 1.494 Å. About 2 g of the sample was contained in a vanadium can. The measurements were carried out at 25 °C (RT). The counting time for each pattern was 3 h. The crystal structures were analyzed by the Rietveld method [24], using the FULLPROF refinement program [25]. The peak profiles were modeled by a pseudo-Voigt function. The following parameters were refined in the final runs: scale factor, background coefficients, zero-point error, pseudo-Voigt corrected for asymmetry parameters, unit-cell parameters, and positional, isotropic thermal factors for the metals and anisotropic for O1 and O2 oxygen atoms. Occupancy factors for oxygen atoms were also refined for NPD data. The coherent scattering lengths for La, Sr, In, Ba, and O were 8.240, 7.020, 4.065, 5.070, and 5.803 fermi, respectively.

2.3. Conductivity Measurements

Solid bars (0.08 × 0.3 × 0.8 cm) were subjected to 2-probe DC conductivity measurements using Pt ink (PSI supplies) as the current collector. Conductivity values were acquired with an Agilent 34972A Data Acquisition Unit at a temperature range between room temperature and 1000 °C under atmospheric air [26].

3. Results and Discussion

3.1. Crystallographic Characterization

The samples were obtained as polycrystalline, yellowish powders. Figure 1 illustrates the laboratory XRD diagrams at room temperature for the three members of the $La_{1.2}Sr_{0.8-x}Ba_xInO_4$ series. The patterns correspond to layered perovskites that can be indexed in the orthorhombic *Pbca* space group (Card 04-017-3962 ICDD). A small amount of La_2O_3 was found (Card 01-073-2141 ICSD) in all patterns.

A neutron diffraction study was essential to reveal the structural features of the three materials. The crystal structures can be defined in the *Pbca* structural model, as proposed by Titov et al. [27]. The A-type metal atoms, La, Sr, and Ba, are statistically distributed over 8c (x,y, z) positions; In atoms occupy the 4b (1/2,0,0) sites and the two types of oxygen atoms O1 and O2 are placed at two distinct 8c Wyckoff sites. The initial refinement of the unit-cell parameters (Table 1) demonstrated a monotonous increase of the unit-cell volume for x = 0.2 (435.23(5) $Å^3$) and 0.3 (437.15(7) $Å^3$) with respect to the parent $La_{1.2}Sr_{0.8}InO_4$ (432.42(4) $Å^3$, [23]), as it corresponds to the larger size of Ba^{2+} vs. Sr^{2+}.

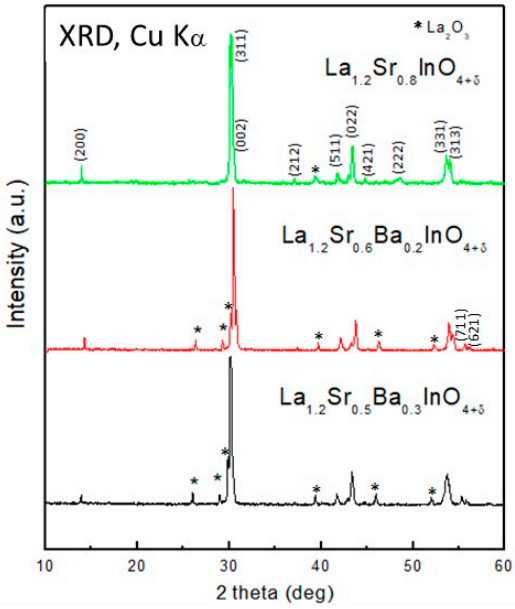

Figure 1. XRD patterns of the materials of the series $La_{1.2}Sr_{0.8-x}Ba_xInO_{4+\delta}$, collected with CuK_α radiation. The stars correspond to La_2O_3 impurity phase.

Table 1. Unit-cell parameters and volume at room temperature for $La_{1.2}Sr_{0.8-x}Ba_xInO_4$.

Reticular Parameters	0.0 *	0.2	0.3	0.4
a (Å)	12.6085(6)	12.6267(9)	12.640(1)	12.635(2)
b (Å)	5.8789(3)	5.9000(4)	5.9073(5)	5.9016(8)
c (Å)	5.8338(3)	5.8421(4)	5.8546(6)	5.863(1)
V (Å^3)	432.42(4)	435.23(5)	437.15(7)	437.22(11)

* From Reference [23].

However, a further increase in the amount of Ba to x= 0.4 does not lead to a significant increment of the unit-cell volume, which indicates that the layered perovskites cannot be further enriched with this element. In the following, only the x = 0.2 and 0.3 materials will be considered. For them, the refinement of the occupancy factor of O1 atoms yielded full stoichiometry whereas O2 displayed the presence of vacancies at the octahedral lattice; O2 are the axial oxygen atoms of the InO_6 octahedra. Additionally, difference Fourier maps allowed the localization of extra interstitial oxygen atoms at 8c (x,y,z) sites, x ≈ y ≈ z ≈ 0.25, as positive peaks (Figure 2 for x = 0.2) placed at the NaCl layers.

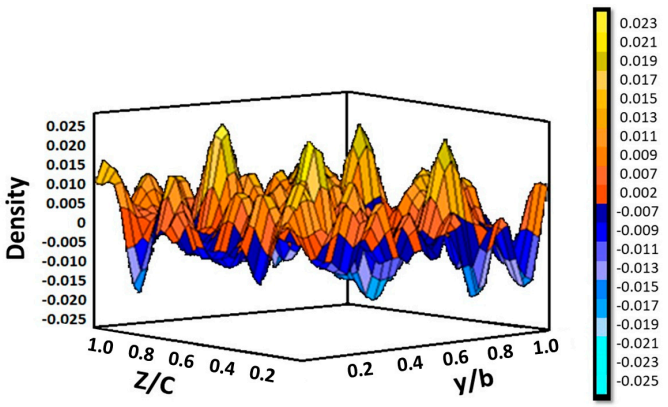

Figure 2. Localization by difference Fourier analysis of the interstitial oxygen atoms (O3) at 8*c* (x,y,z) sites, corresponding to the x = 0.22 layer, for $La_{1.2}Sr_{0.6}Ba_{0.2}InO_{4+\delta}$ from neutron powder diffraction (NPD) data at room temperature.

Once introduced in the structural model as O3 atoms, a significant decrease of the R_{Bragg} discrepancy factors from 7.5% to values below 6% was observed. The combination of oxygen vacancies on O2 sites and interstitial O3 atoms yields a global oxygen stoichiometry of 4.10(2), as expected from the metal charge misbalance between La^{3+}, Sr^{2+} and Ba^{2+}. A minor impurity phase of La_2O_3 was detected in all the patterns and included in the refinement as a second phase. Figure 3a,b illustrates the quality of the Rietveld fits for $La_{1.2}Sr_{0.6}Ba_{0.2}InO_{4.10(2)}$ and $La_{1.2}Sr_{0.5}Ba_{0.3}InO_{4.10(2)}$. Table 2 contains the main atomic parameters after the refinement; Table 3 lists the anisotropic displacement parameters for O2 and O3 and Table 4 the main interatomic distances and bond angles.

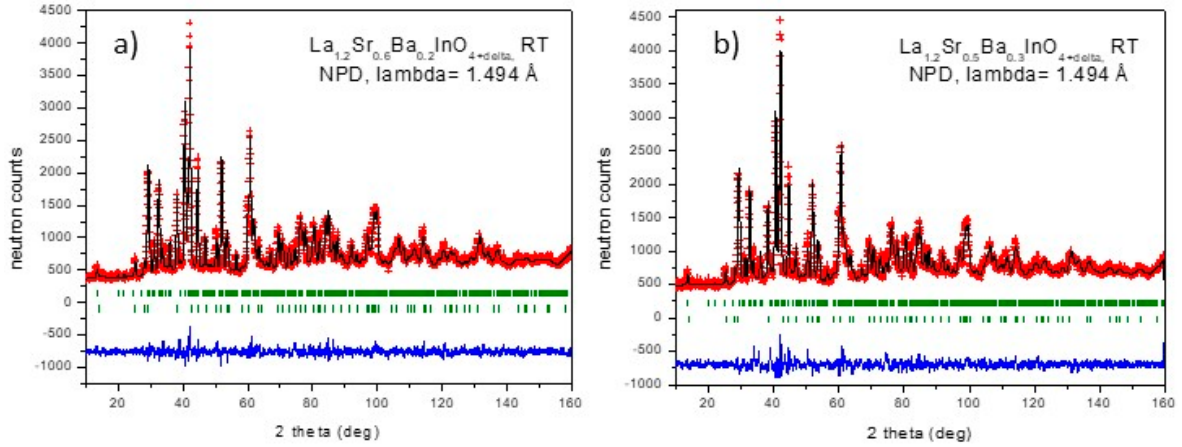

Figure 3. Observed (crosses), calculated (full line) and difference (at the bottom) NPD profiles for (**a**) $La_{1.2}Sr_{0.6}Ba_{0.2}InO_{4+\delta}$, and (**b**) $La_{1.2}Sr_{0.5}Ba_{0.3}InO_{4+\delta}$, at 25 °C, refined in the *Pbca* space group. The vertical markers correspond to the allowed Bragg reflections for the main phase; the second series of markers corresponds to La_2O_3 minor impurity phase.

Table 2. Structural parameters and discrepancy factors after the Rietveld refinement of $La_{1.2}Sr_{0.6}Ba_{0.2}InO_{4+\delta}$ in the space group *Pbca* from NPD data.

Atoms		x = 0.0 *	x = 0.2	x = 0.3
La/Sr/Ba 8c (x,y,z)	x	0.1458(8)	0.1469(8)	0.1463(1)
	y	−0.0155(2)	−0.0146(3)	−0.0124(4)
	z	0.9726(2)	0.9928(6)	1.0019(9)
	B(Å^2)	1.14(5)	1.52(1)	1.51(7)
	focc	0.59(1)/0.41(1)	0.6/0.3/0.1	0.6/0.25/0.15
In 4b (1/2 0 0)	B(Å^2)	0.69(11)	0.60(1)	0.68(13)
	focc	1.0	1.0	1.0
O1 8c (x,y,z)	x	0.0269(1)	0.0219(2)	0.0199(3)
	y	0.2161(3)	0.2322(5)	0.2407(1)
	z	0.2120(5)	0.2224(4)	0.2267(6)
	focc	1.0	1.0	1.0
O2 8c (x,y,z)	x	0.3268(1)	0.3236(2)	0.3251(3)
	y	0.0807(3)	0.0752(4)	0.0672(6)
	z	0.0301(4)	0.0146(9)	−0.0142(5)
	focc	1.0	0.897(2)	0.906(3)
O3 8c (x,y,z)	x	0.216(2)	0.2135(8)	0.2009(2)
	y	0.249(5)	0.2393(4)	0.2217(1)
	z	0.267(5)	0.1901(4)	0.2196(9)
	B(Å^2)	3.88(1)	3.4(3)	6.6(1)
	focc	0.054(6)	0.103(2)	0.144(3)
Discrepancy Factors	χ^2	2.80	2.36	2.72
	R_p (%)	4.44	4.39	4.38
	R_{wp} (%)	5.96	5.61	5.71
	R_{Bragg} (%)	5.98	5.97	6.93

* From Reference [23].

Table 3. Anisotropic displacement factors for O1 and O2 in $La_{1.2}Sr_{0.6}Ba_{0.2}InO_{4+\delta}$ from NPD data.

Atom	x	0.0 *	0.2	0.3
O1 8c (x,y,z)	β_{11}	26(3)	71(5)	109(8)
	β_{22}	61(10)	14(11)	81(16)
	β_{33}	126(13)	111(14)	122(19)
	β_{12}	−27(5)	5(9)	16(22)
	β_{13}	5(5)	−5(8)	72(17)
	β_{23}	44(10)	30(0)	70(0)
O2 8c (x,y,z)	β_{11}	16(2)	35(3)	49(5)
	β_{22}	57(9)	79(11)	129(18)
	β_{33}	262(15)	279(22)	478(42)
	β_{12}	13(4)	17(5)	−14(9)
	β_{13}	16(6)	−36(15)	−85(22)
	β_{23}	20(11)	−44(22)	175(37)

* From Reference [23].

Table 4. Main interatomic distances (Å) and angles (°) for $La_{1+x}Sr_{1-x}In_{4+\delta}$ (x = 0.0, 0.2, and 0.3) determined from NPD data at RT.

x	0.0 *	0.2	0.3
La/Sr/Ba–O1	2.468(2)	2.532(3)	2.553(6)
La/Sr/Ba–O1	2.695(2)	3.089(3)	3.011(6)
La/Sr/Ba–O1	2.767(2)	2.788(3)	2.832(5)
La/Sr/Ba–O1		2.786(4)	2.779(6)
La/Sr/Ba–O2	2.366(2)	2.297(3)	2.311(4)
La/Sr/Ba–O2	2.636(3)	2.841(6)	3.060(10)
La/Sr/Ba–O2	2.425(2)	3.092(6)	2.874(10)
La/Sr/Ba–O2		2.452(3)	2.511(4)
La/Sr/Ba–O3	2.621(5)	2.067(12)	2.01(5)
La/Sr/Ba–O3	2.694(4)	2.827(11)	2.83(4)
La/Sr/Ba–O3	2.81(2)	2.559(11)	2.80(4)
La/Sr/Ba–O3	2.15(2)	2.546(12)	2.48(5)
In–O1 (x2)	2.115(2)	2.064(3)	2.042(5)
In–O1 (x2)	2.122(2)	2.141(3)	2.155(5)
In–O2 (x2)	2.249(2)	2.273(3)	2.248(4)
In–O1–In	155.55(8)	161.68(10)	164.34(19)

* From Reference [23].

Figure 4 shows two views of the orthorhombic crystal structure for x = 0.3 at RT, consisting of layers of rotated InO_6 octahedra alternating with (La/Sr/Ba)–O layers with NaCl structure.

The InO_6 octahedra are significantly tilted by θ = 9.16° and 7.83° for x = 0.2 and 0.3, respectively (Table 4), obtained as θ = [180 − (In–Ô–In)]/2. The reduction of the tilting angle is expected for a structure with a higher tolerance factor determined by the larger ionic size of Ba^{2+} with respect to La^{3+} or Sr^{2+}. The interstitial O3 atoms occupying the NaCl layer are bonded to (La, Sr) with reasonable distances of 2.50 Å (in average) range.

In this respect, a last issue concerns the mechanism that can be induced from the structural features determined by neutron diffraction for both perovskite oxides. In principle, it is believed that the ionic transport required for the performance of the electrolyte materials for SOFC works with a vacancy mechanism, the pre-existing vacancies being filled by neighboring oxygen atoms upon conduction of oxide ions. However, in this case, the neutron data consistently indicate, for both compounds at RT, that the layered perovskites contain both oxygen vacancies located at the axial oxygen atoms of the InO_6 octahedra as well as interstitial oxygens conspicuously located in the NaCl layers. As it is plausible that all these materials combine an excellent ionic conductivity with a sufficient ionic transport of oxide anions, as demonstrated for the parent $La_{1+x}Sr_{1-x}InO_{4+\delta}$ materials [23], we could imagine a mixed

mechanism where the existing vacancies at O2 are filled with O3 atoms and with no steric impediment, giving rise to a fast transport of oxide ions across the NaCl layers. The large values of the displacement parameters (Table 3) for O3 and the anisotropic, cigar-shaped anisotropic displacement parameters (ADPs) for axial O2 oxygens are a fixed picture of a dynamic situation involving very reactive atoms, the lability being induced by the presence of very basic Ba^{2+} ions prone to form weak covalent bonds to oxygen.

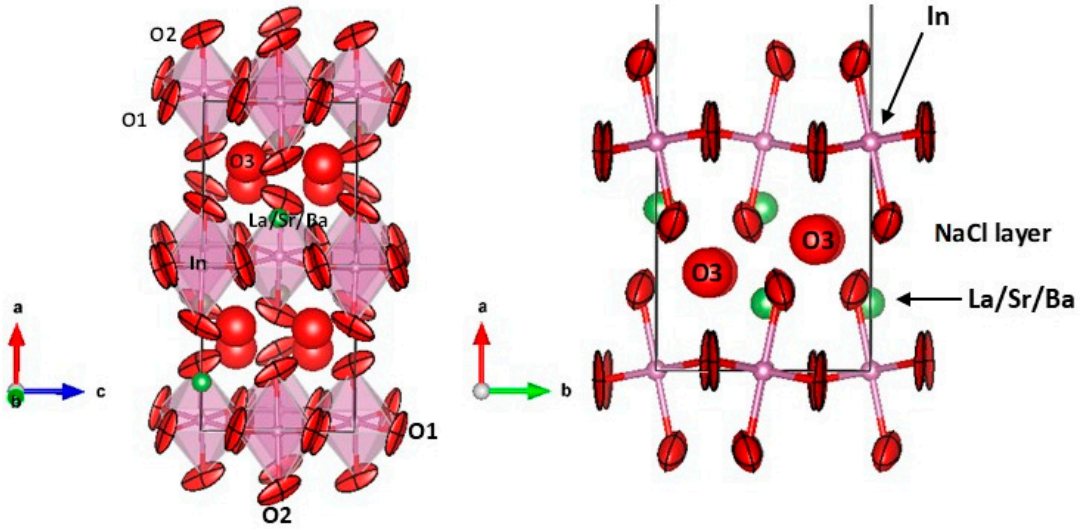

Figure 4. Crystal structure views of $La_{1.2}Sr_{0.5}Ba_{0.3}InO_{4+\delta}$, showing sheets of tilted InO_6 octahedra alternating with (La/Sr/Ba)–O layers, where interstitial O3 oxygen atoms are located, highlighting the anisotropic displacement parameters, of oblate type for equatorial O1 and prolate type for axial O2 oxygen atoms. The ellipsoids are represented with 95% of probability. The right panel highlights the NaCl layer where O3 interstitials are accommodated taking advantage of the space left by the octahedral tilting. Figures were made using the VESTA program.

3.2. Electrical Conductivity Measurements

The total conductivity was measured to compare our samples with the parent $La_{1.2}Sr_{0.8}InO_{4.11}$ [23]. The results show a classical behavior of ionic conductivity in ceramic materials: It is a thermally activated or Arrhenius-type process given by Equation (1), where σ is the conductivity in (S/cm), T is the absolute temperature in (K), A is a pre-exponential factor, Ea is the activation energy in (J) and k_B is the Boltzmann constant in (J/K).

$$\sigma(T) = Ae^{-Ea/k_BT} \quad (1)$$

Figure 5 shows the graph of the thermal variation of total conductivity (σ) in air for $La_{1.2}Sr_{0.8-x}Ba_xInO_{4+\delta}$ (x = 0.0, 0.1, 0.2) compared with that of commercial electrolytes. The parent sample (x = 0.0), as reported in Reference [23], shows an unusually low activation energy (0.51 eV) in the range between 500 and 700 °C, where a change of slope occurs, making it competitive with the electrolytes of $La_{1-x}Sr_xGa_{1-y}Mg_yO_{3-\delta}$, $Ce_{1-x}GdO_{2-\delta}$ and $Zr_{1-x}Y_xO_{2-\delta}$, at low temperatures. In that case [23], NDP data proved no oxygen vacancies inside the structure. The Ba-doped oxides present values of Ea = 1.00 eV, for both x = 0.2 and 0.3. The activation energy values are similar to those typically exhibited by ionic conductors working by a vacancy mechanism (~1 eV), but as shown in Figure 5, they are still several orders of magnitude lower in conductivity than commercial electrolytes. Although, in the case of these barium-doped samples, there is no evidence of changes in the activation energy as in the parent compound, the sample $La_{1.2}Sr_{0.6}Ba_{0.2}InO_{4.10}$ increases by 1 order of magnitude its conductivity, and at low temperatures, the tendency to be competitive with the typical electrolytes remains. In Table 2, it is observed that the occupation of the interstitial oxygens (O3) doubles the

amount observed in the parent compound, due to the extra space provided by the insertion of the Ba cation, and at the same time, it presents an appreciable amount of vacancies at O2 sites. The increase in conductivity can be a result of the mixed mechanism driven by the presence of both oxygen vacancies and interstitials.

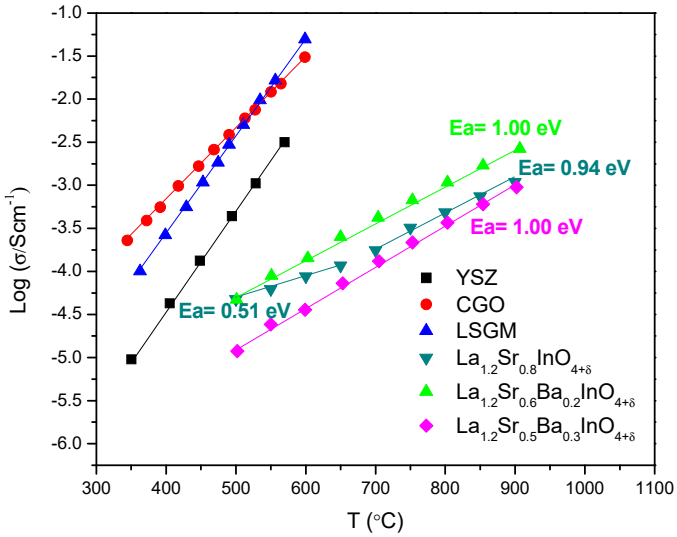

Figure 5. Conductivity for different electrolytes compared to $La_{1.2}Sr_{0.8-x}Ba_xInO_{4+d}$ Reference [23].

In other words, the layered perovskite of $La_{1.2}Sr_{0.6}Ba_{0.2}InO_{4.10}$ is among the few oxides containing a measurable concentration of permanent vacancies as well as adjacent interstitial atoms in the interlayer space, which together can participate in the conduction mechanism to ensure a fast ionic transport.

4. Conclusions

$La_{1+x}Sr_{1-x}InO_{4+\delta}$ layered perovskites have recently been described as suitable candidates for electrolyte materials in SOFCs [22,23]. Based on the material with the best properties, $La_{1.2}Sr_{0.8}InO_{4+\delta}$, which contains a substantial amount of interstitial oxygen atoms that easily move in the interlayer plane, here we designed a unique series containing Ba^{2+} ions. Its larger ionic size drives the expansion of the unit cell, where a better oxygen conduction is expected. A neutron diffraction study reveals novel and unexpected features, since oxygen vacancies at the axial O2 octahedral positions were detected, besides the interstitial oxygen atoms located in the NaCl-type layer. Difference Fourier maps from NPD data at RT clearly show prominent positive peaks corresponding to the O3 interstitial oxygen atoms; the short distances with the oxygen vacancies make possible a dual jump mechanism where both point defects participate. Moreover, the strongly anisotropic, cigar-shaped ellipsoids for O2 mimic the displacement of axial oxygen atoms in the interlayer space, also anticipating an excellent ionic motion for oxide ions. The low activation energies measured for x = 0.2 and x = 0.3 compounds endorses this hypothesis. The presence of Ba ions in this novel series, besides the forecasted expansion of the framework, induces a second beneficial effect: the basic character of these cations, more prone to form weaker chemical bonds, favor the formation of oxygen vacancies in a crystal structure involving very labile atoms where oxygen conduction is promoted in the (La,Sr,Ba)–O (NaCl-type) layers.

Author Contributions: Conceptualization, J.A.A. and L.T.; Funding acquisition, J.A.A. and L.T.; Investigation, J.A.A., L.T., C.M. and M.D.A.; Methodology, J.A.A. and L.T.; Project administration, J.A.A. and L.T.; Resources, J.A.A., L.T. and M.D.A.; Writing—original draft, J.A.A., L.T. and C.M.; Writing—review & editing, J.A.A. and L.T.

Funding: J.A.A. thanks the Spanish Ministry of Economy and Competitivity for granting the project MAT2017-84496-R, and PSI-SINQ for making all facilities available for the neutron diffraction experiments. L.T. and C.M. thanks the support from CONICYT Chile (Fondecyt grant 11170068) and M.D.A. thanks CONICET (PICT 2016-2965) and CNEA for the financial support.

Conflicts of Interest: The authors declare no conflicts of interest.

References

1. Lutz, A.E.; Larson, R.S.; Keller, J.O. Thermodynamic comparison of fuel cells to the Carnot cycle. *Int. J. Hydrogen Energy* **2002**, *27*, 1103–1111. [CrossRef]
2. Ramadhani, F.; Hussain, M.A.; Mokhlis, H.; Hajimolana, S. Optimization strategies for Solid Oxide Fuel Cell (SOFC) application: A literature survey. *Renew. Sust. Energ Rev.* **2017**, *76*, 460–484. [CrossRef]
3. Choudhary, T.; Kumar Sahu, M. CFD Modeling of SOFC Cogeneration System for Building Application. *Energy Procedia* **2017**, *109*, 361–368. [CrossRef]
4. Wilberforce, T.; Alaswad, A.; Palumbo, A.; Dassisti, M.; Olabi, A.G. Advances in stationary and portable fuel cell applications. *Int. J. Hydrogen Energy* **2016**, *41*, 16509–16522. [CrossRef]
5. Badwal, S.P.S. Zirconia-based solid electrolytes: microstructure, stability and ionic conductivity. *Solid State Ionics* **1992**, *52*, 23–32. [CrossRef]
6. Steele, B.C. Appraisal of $Ce_{1-y}Gd_yO_{2-y/2}$ electrolytes for IT-SOFC operation at 500° C. *Solid State Ionics* **2000**, *129*, 95–110. [CrossRef]
7. Huang, K.; Tichy, R.S.; Goodenough, J.B. Superior perovskite oxide-ion conductor; strontium-and magnesium-doped $LaGaO_3$: I, phase relationships and electrical properties. *J. Am. Ceram. Soc.* **1998**, *81*, 2565–2575. [CrossRef]
8. Wang, Z.; Wang, X.; Xu, Z.; Deng, H.; Dong, W.; Wang, B.; Wang, H. Semiconductor-Ionic Nanocomposite $La_{0.1}Sr_{0.9}MnO_{3-\delta}$-$Ce_{0.8}Sm_{0.2}O_{2-\delta}$ Functional Layer for High Performance Low Temperature SOFC. *Materials* **2018**, *11*, 1549. [CrossRef]
9. Benes, A.; Molinari, A.; Witte, R.; Kruk, R.; Brötz, J.; Chellali, R.; Clemens, O. Proton Conduction in Grain-Boundary-Free Oxygen-Deficient $BaFeO_{2.5+\delta}$ Thin Films. *Materials* **2017**, *11*, 52. [CrossRef]
10. Accardo, G.; Dell'Agli, G.; Mascolo, M.C.; Spiridigliozzi, L.; Yoon, S.P. Controlled Coprecipitation of Amorphous Cerium-Based Carbonates with Suitable Morphology as Precursors of Ceramic Electrolytes for IT-SOFCs. *Materials* **2019**, *12*, 702. [CrossRef]
11. Lai, Y.W.; Wei, W.C. Synthesis and Study on Ionic Conductive (Bi_{1-x}, V_x) $O_{1.5-\delta}$ Materials with a Dual-Phase Microstructure. *Materials* **2016**, *9*, 863. [CrossRef] [PubMed]
12. Perry, N.; Ishihara, T. Roles of bulk and surface chemistry in the oxygen exchange kinetics and related properties of mixed conducting perovskite oxide electrodes. *Materials* **2016**, *9*, 858. [CrossRef] [PubMed]
13. Santos, T.H.; Grilo, J.P.; Loureiro, F.J.; Fagg, D.P.; Fonseca, F.C.; Macedo, D.A. Structure, densification and electrical properties of Gd^{3+} and Cu^{2+} co-doped ceria solid electrolytes for SOFC applications: Effects of Gd_2O_3 content. *Ceram. Int.* **2018**, *44*, 2745–2751. [CrossRef]
14. Bi, L.; Da'as, E.H.; Shafi, S.P. Proton-conducting solid oxide fuel cell (SOFC) with Y-doped $BaZrO_3$ electrolyte. *Electrochem. Commun.* **2017**, *80*, 20–23. [CrossRef]
15. Béchade, E.; Masson, O.; Iwata, T.; Julien, I.; Fukuda, K.; Thomas, P.; Champion, E. Diffusion path and conduction mechanism of oxide ions in apatite-type lanthanum silicates. *Chem. Mater.* **2009**, *21*, 2508–2517. [CrossRef]
16. Bhosale, D.R.; Yusuf, S.M.; Kumar, A.; Mukadam, M.D.; Patil, S.I. High oxide ion conductivity below 500 °C in the garnets $La_xY_{3-x}Fe_5O_{12+\delta}$. *Phys. Rev. Mater.* **2017**, *1*, 015001. [CrossRef]
17. Berger, C.; Bucher, E.; Egger, A.; Strasser, A.T.; Schrödl, N.; Gspan, C.; Sitte, W. Synthesis and characterization of the novel K_2NiF_4-type oxide $Pr_2Ni_{0.9}Co_{0.1}O_{4+\delta}$. *Solid State Ionics* **2018**, *316*, 93–101. [CrossRef]
18. Yang, G.; Su, C.; Ran, R.; Tade, M.O.; Shao, Z. Advanced symmetric solid oxide fuel cell with an infiltrated K_2NiF_4-type La_2NiO_4 electrode. *Energy Fuels* **2014**, *28*, 356–362. [CrossRef]
19. Sayers, R.; Liu, J.; Rustumji, B.; Skinner, S.J. Novel K_2NiF_4-type materials for solid oxide fuel cells: Compatibility with electrolytes in the intermediate temperature range. *Fuel Cells* **2008**, *8*, 338–343. [CrossRef]
20. Lee, D.; Lee, H. Controlling oxygen mobility in Ruddlesden–Popper oxides. *Materials* **2017**, *10*, 368. [CrossRef]
21. Skinner, S.J.; Kilner, J.A. Oxygen ion conductors. *Mater. Today* **2003**, *6*, 30–37. [CrossRef]
22. Troncoso, L.; Alonso, J.A.; Fernández-Díaz, M.T.; Aguadero, A. Introduction of interstitial oxygen atoms in the layered perovskite $LaSrIn_{1-x}B_xO_{4+\delta}$ system (B = Zr, Ti). *Solid State Ionics* **2015**, *282*, 82–87. [CrossRef]
23. Troncoso, L.; Alonso, J.A.; Aguadero, A. Low activation energies for interstitial oxygen conduction in the layered perovskites $La_{1+x}Sr_{1-x}InO_{4+\delta}$. *J. Mater. Chem. A* **2015**, *3*, 17797–17803. [CrossRef]
24. Rietveld, H. A profile refinement method for nuclear and magnetic structures. *J. Appl. Crystallogr.* **1969**, *2*, 65–71. [CrossRef]

25. Rodríguez-Carvajal, J. Recent advances in magnetic structure determination by neutron powder diffraction. *Phys. B Condensed Matter* **1993**, *192*, 55–69. [CrossRef]
26. Caneiro, A.; Bavdaz, P.; Fouletier, J.; Abriata, J.P. Adaptation of an electrochemical system for measurement and regulation of oxygen partial pressure to a symmetrical thermogravimetric analysis system developed using a Cahn 1000 electrobalance. *Rev. Sci. Instrum.* **1982**, *53*, 1072–1075. [CrossRef]
27. Yu, A.; Titov, N.M.; Belyavina, V.; Ya Markiv, M.S.; Slobodyanik, Y.; Krayevska, A. Synthesis and crystal structure of $BaLaInO_4$ and $SrLnInO_4$ (Ln—La, Pr). *Dopov. Nats. Akad. Nauk. Ukr.* **2009**, *160*, 166.